1

Dislocation Formation During Physical Vapor Transport Growth of 4H-SiC Crystals

Noboru Ohtani

Kwansei Gakuin University, School of Engineering, 2-1 Gakuen, Sanda, Hyogo 669-1337, Japan

1.1 Introduction

Silicon carbide (SiC) is the leading candidate among wide-bandgap semiconductor materials for next-generation power semiconductor devices. Over recent decades, the quality of SiC single crystals has improved considerably, thereby making it feasible to fabricate high-performance SiC power devices. 4H-SiC epitaxial wafers of 100 and 150 mm in diameter, with low dislocation density are already available in the market and have been used to fabricate high-performance SiC power devices [1]. However, the widespread commercialization of such devices remains hindered by technological issues related to SiC crystal growth. It is abundantly clear that further successful development of SiC semiconductor technology relies on understanding the process of SiC crystal growth and thus improving the technology for manufacturing large high-quality SiC crystals.

In this chapter, I describe recent progress in understanding the formation of defects during physical vapor transport (PVT) growth of SiC, focusing particularly on the formation of dislocations in 4H-SiC. Currently, commercially available SiC bulk crystals are almost always grown by PVT, namely, by the modified Lely method [2]. However, dislocation formation during the PVT growth of bulk SiC crystals remains a major obstacle to realizing high-performance SiC power devices. Certain types of dislocation are detrimental to the yield and reliability of SiC power devices. Dislocations in PVT-grown SiC crystals are classified broadly into two types, namely, (i) threading dislocations extending along the *c*-axis and (ii) basal plane dislocations (BPDs) lying in the basal plane. Threading dislocations, particularly threading screw dislocations (TSDs), degrade the blocking capabilities of SiC diodes [3–5], whereas BPDs have a serious impact on the reliability of unipolar devices such as SiC metal oxide semiconductor field-effect transistors (MOSFETs) and junction gate field-effect transistors (JFETs) [6, 7] as well as SiC bipolar devices [8, 9]. Therefore, over the decades, considerable effort has gone into reducing the TSD and BPD densities in SiC crystals.

TSDs and BPDs differ markedly in how they form during the PVT growth of SiC crystals. Most TSDs are inherited from the seed crystal and often form in the initial

Wide Bandgap Semiconductors for Power Electronics: Materials, Devices, Applications,
First Edition. Edited by Peter Wellmann, Noboru Ohtani, and Roland Rupp.

stage of crystal growth [10–12]. BPDs can also be inherited from the seed crystal and form during the initial seeding process, but they do not propagate throughout the entire crystal because their propagation or extension directions are restricted to the basal plane, almost normal to the growth direction. Therefore, the high density of BPDs in the top and middle portions of SiC crystals cannot be explained by the aforementioned mechanisms, and the causes of the BPDs observed in these portions remain poorly understood.

A plausible explanation is that BPDs are nucleated at the growth front (growing crystal surface) and then incorporated into the growing crystal. In general, defect formation at the growth front is closely related to the shape and morphology of the growing crystal surface; the crystal shape determines the magnitude and distribution of the thermoelastic stresses imposed on the grown crystals [13–16], and the surface morphology at the growth front largely affects the defect formation kinetics. Therefore, control of these growth parameters is crucial to obtain high-quality SiC single crystals.

In Section 1.2, I discuss the BPD formation during the PVT growth of 4H-SiC crystals. SiC single crystals of the 4H polytype are the ones studied and implemented most intensively by the industry. The present author's group investigated the BPD formation by characterizing the BPD distributions at the growth front as well as inside 4H-SiC single-crystal boules grown by PVT. The investigation was focused to identify where and how BPDs are nucleated and multiplied in PVT-grown 4H-SiC crystals. As described earlier, the growth front of 4H-SiC crystals is the most plausible location where BPDs are nucleated. The growth front comprises the $(000\bar{1})$ facet and its outer (non-facet [NF]) regions; they exhibit characteristic surface morphologies in terms of the step-terrace structure. The morphologies of these two regions are quite different [17, 18], and thus different defect formation kinetics would govern the defect formation on the two surface regions. Furthermore, these two regions grow into different crystal shapes; the facet is fairly flat and has a temperature distribution across the surface during PVT growth [18], whereas the non-facet regions are convex-shaped toward the growth direction and are assumed to be roughly isothermal during growth [19]. The degree of the convexity of the growth front is also a crucial parameter for defect formation during the PVT growth of SiC. As such, investigating the crystalline properties of the facet and non-facet regions at the growth front provides valuable information about the formation of defects during the PVT growth of SiC crystals.

As described earlier in this section, another relevant issue for dislocation formation during the PVT growth of 4H-SiC crystals is the seeding process. In general, the seeding process, namely, how crystal growth is initiated on the seed crystal, is a key issue for reproducible growth of high-quality single crystals. This is also true for the PVT growth of 4H-SiC single crystals, and thus, establishing a well-controlled seeding process for the PVT growth of SiC is necessary for obtaining high-quality 4H-SiC bulk single crystals. Several authors have tried to reveal the growth mode and the defect formation process during the initial stage of PVT growth [10–12, 20–25]. However, detailed knowledge about the seeding process of SiC PVT growth remains lacking, and further intensive study is required to explore

this important technological issue in SiC PVT growth. An obstacle to investigating the seeding process of SiC PVT growth is that defect formation occurs within a very narrow range near the interface between the seed and grown crystal, and this greatly hinders detailed observations and analyses of the defect formation at the interface.

Another reason why it is difficult to study the defect formation at and near the grown-crystal/seed interface is the complexity of causes of defect formation during the initial stage of SiC PVT growth, such as thermoelastic stress [10, 12], growth kinetics [10, 11, 21], surface conditions of the seed crystal [20], and nitrogen doping enrichment near the grown-crystal/seed interface [12, 22–25]. Section 1.3 is dedicated to this issue, and recent studies of the dislocation formation at the grown-crystal/seed interface during PVT growth of 4H-SiC crystals are described. Slightly off-oriented $(000\bar{1})$ wafers containing the beveled interface between the grown crystal and seed crystal were prepared, which revealed a characteristic dislocation structure formed at the interface and indicated the important role of vacancy injection during the initial stage of the PVT growth of 4H-SiC crystals.

In Section 1.4, I summarize this chapter and draw some conclusions.

1.2 Formation of Basal Plane Dislocations During PVT Growth of 4H-SiC Crystals

1.2.1 Plan-View X-ray Topography Observations of Growth Front

Figure 1.1 shows schematically (a) the PVT growth reactor of 4H-SiC crystals and (b) the scheme for preparing the top portion of the grown crystal with the $(000\bar{1})$ facet and a 4H-SiC $(1\bar{1}00)$ or $(11\bar{2}0)$ wafer sliced vertically along the growth direction from a 4H-SiC single crystal. The crystal was grown on an on-axis or off-oriented 4H-SiC $(000\bar{1})$C seed crystal. The vertically sliced $(1\bar{1}00)$ or $(11\bar{2}0)$ wafer consisted of two

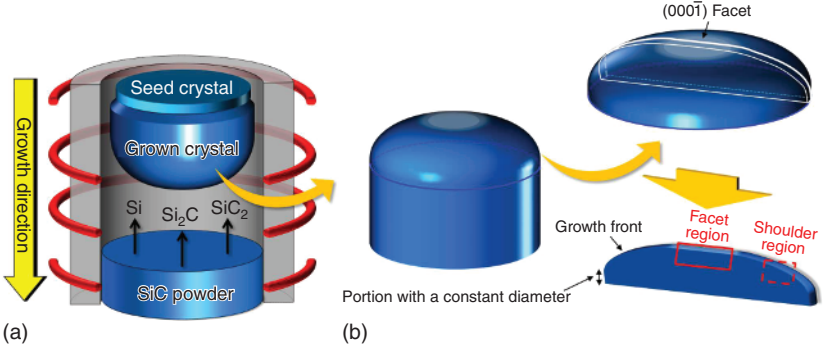

Figure 1.1 Schematics of (a) physical vapor transport (PVT) growth reactor and (b) preparation scheme of top portion of grown crystal with $(000\bar{1})$ facet and a 4H-SiC $(1\bar{1}00)$ or $(11\bar{2}0)$ wafer sliced vertically in the growth direction from a 4H-SiC single-crystal boule grown on a 4H-SiC $(000\bar{1})$C seed crystal. The areas in the wafer examined by transmission X-ray topography are indicated by red open rectangles. Source: Nakano et al. [26]. © 2019, Elsevier.

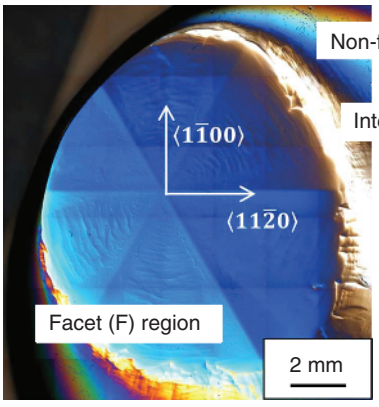

Figure 1.2 Differential interference contrast (DIC) optical microscopy image of growth front of nitrogen-doped (mid-10^{18} cm^{-3}) 4H-SiC single-crystal boule examined in this study. The growth front consists of three distinct morphological regions, namely, the (000$\bar{1}$)C facet (F) and non-facet (NF) regions and the intermediate (I) region between them (after [27]). Source: Sonoda et al.

portions that are classified from the perspective of crystal growth. One was accompanied by the growth front that showed a domed shape (convex toward the growth direction). In this portion, crystal growth occurred during PVT growth. The other portion contained the side surfaces of the crystal, on which there was nominally no crystal growth, and thus it had a constant diameter.

Figure 1.2 shows a differential interference contrast (DIC) optical microscopy image of the growth front of a nitrogen-doped (mid-10^{18} cm^{-3}) 4H-SiC boule examined by Sonoda et al. [27]. The figure reveals that the growth front of the nitrogen-doped 4H-SiC single-crystal boule comprised three distinct morphological regions, namely, (i) the (000$\bar{1}$)C facet region (denoted as F in the figure), (ii) the non-facet (NF) region, and (iii) the intermediate (I) region between F and NF. The facet region exhibited hexagonal symmetry comprising six vicinal (000$\bar{1}$)C surfaces tilted toward the <1$\bar{1}$00> direction. The vicinal surfaces were separated by six crystallographically equivalent ridges extending along the <11$\bar{2}$0> direction. The non-facet region exhibited macroscopically smooth morphology, and the convexity of the region varied depending on the growth conditions, particularly, the temperature distribution in the growth cell. The intermediate region was arranged on the perimeter of the facet region, was narrow, and exhibited a macroscopically slightly rough morphology.

Figure 1.3 shows reflection X-ray topographs of the growth front of a nitrogen-doped 4H-SiC boule in the diffraction conditions (a) $\boldsymbol{g} = 11\bar{2}\bar{8}$ and (b) $1\bar{1}0\bar{7}$, obtained by Sonoda et al. [27]. In the topographs, the boundaries of the facet, intermediate, and non-facet regions are marked by dashed lines. Both topographs contain relatively intense linear contrasts extending roughly along the <1$\bar{1}$00> direction; some of them are marked with open triangles in the topographs. They correspond to low-angle grain boundaries consisting of threading edge dislocations (TEDs) penetrating the crystal along the *c*-axis. Small dot-like contrasts were also observed in both topographs. They had two possible origins, namely, TSDs and TEDs, but were ascribed to TSDs based on their estimated density (~10^3 cm^{-2}). As shown in Figure 1.3, no marked difference in the defect structure was found among the three regions of the as-grown surface, namely, the facet, intermediate,

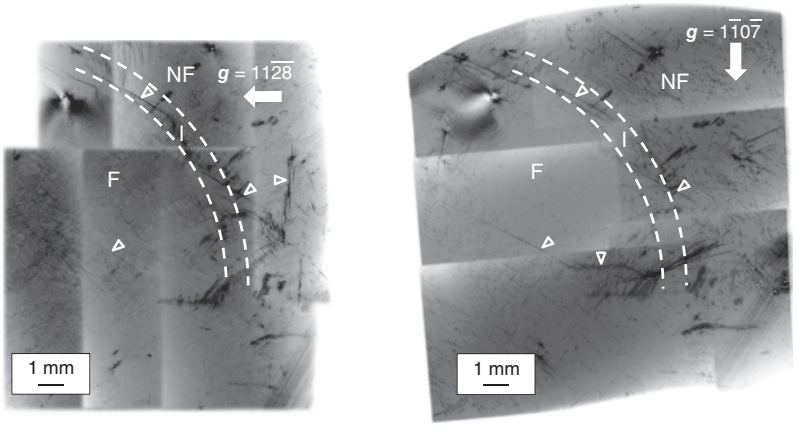

Figure 1.3 Reflection X-ray topographs from the three regions at the growth front of a PVT-grown 4H-SiC crystal. The diffraction vector was (a) $11\bar{2}\bar{8}$ and (b) $1\bar{1}0\bar{7}$. In the topographs, the facet, non-facet, and intermediate regions are denoted as F, NF, and I, respectively, and their boundaries are marked by dashed lines. Source: Sonoda et al. [27].

and non-facet regions, implying that the faceted growth front hardly affects the formation of extended defects during PVT growth of 4H-SiC boules.

The topographs with diffraction vectors $\boldsymbol{g} = 11\bar{2}\bar{8}$ and $1\bar{1}0\bar{7}$ shown in Figure 1.3a,b exhibit slightly different image textures. This is thought to be due to BPDs existing in the crystal portion just beneath the as-grown surface of the boule. BPDs, which have Burger vectors within the basal plane, are out of contrast when the diffraction vector is perpendicular to their Burgers vector, and thus, the two topographs taken with different diffraction vectors exhibit slightly different contrast patterns (image textures).

Figure 1.4 shows enlarged X-ray topographs for more detailed investigation of the dislocation structure underneath the facet and near-facet regions [27]. In the figure, wider-area topographs (Figure 1.4a,c) are also presented, in which the $(000\bar{1})$ facet region is marked by a white circle, and the positions at which the enlarged X-ray topographs (Figure 1.4b,d) were taken are indicated by open squares. The topographs shown in Figure 1.4a,b were taken with the diffraction vector $\boldsymbol{g} = 11\bar{2}\bar{8}$, whereas those in Figure 1.4c,d were taken in the diffraction vector $\boldsymbol{g} = 1\bar{1}0\bar{7}$. Figure 1.4b,d was acquired from the same area in the as-grown crystal surface of a 4H-SiC single-crystal boule (indicated by open squares in Figure 1.4a,c). In Figure 1.4b, both TSDs and BPDs were observed; they are indicated by closed and open triangles, respectively. By contrast, only TSDs were detected in Figure 1.4d in which BPDs exhibited no distinct contrast because the diffraction vector was set perpendicular to their Burgers vectors. These observations indicate that at this particular region of the grown crystal, most BPDs had the same Burgers vector, which implies that they arose from the same cause during the PVT growth process.

In Figure 1.4b, note that many of the observed BPDs seem to emanate from TSDs. Sonoda et al. examined other areas on the as-grown surface and found similar cases of BPDs emanating from TSDs [27]. These results suggest that the existence of

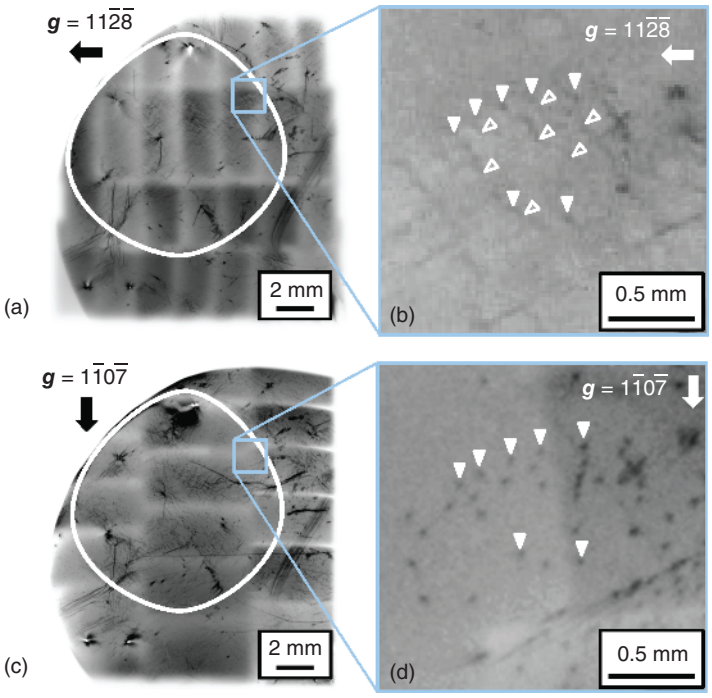

Figure 1.4 Reflection X-ray topographs of the growth front in the diffraction conditions (a) $\boldsymbol{g} = 11\bar{2}\bar{8}$ and (c) $1\bar{1}0\bar{7}$. (b, d) Enlarged X-ray topographs of the areas indicated by open squares in (a, c), respectively. In (b, d), some of the dot-like and line contrasts due to threading screw dislocations (TSDs) and basal plane dislocations (BPDs) are marked by closed and open triangles, respectively. Source: Sonoda et al. [27].

TSDs is related to the BPD formation at the growth front, and TSDs intersecting the growing crystal surface would induce the nucleation of BPDs at the surface during PVT growth of 4H-SiC boules. The mechanism is yet to be clarified, but the elastic interaction between TSDs and the growing crystal surface would play a crucial role in this phenomenon. In this respect, Wang et al. reported an important result that is helpful when considering the origin of this phenomenon [28]. They found that BPDs existing in commercially available 6H-SiC substrates connect or emanate from micropipes (super screw dislocations), comprising dislocation networks in the substrates. Similar BPD structures have also been reported in 4H-SiC epitaxial layers [29]. Micropipes and TSDs extending along the *c*-axis in an infinite crystal do not have a shear stress component parallel to the basal plane, and hence, they could not be the cause of BPDs in an infinite crystal. However, in a finite crystal, they interact elastically with the free surface, and the resultant surface relaxation due to the image force effect of dislocations [30] can provide a shear stress parallel to the basal plane. Compared to micropipes, TSDs provide lower shear stress because of their relatively smaller Burgers vector. However, the Burgers vector of TSDs would be still large enough for them to provide a shear stress exceeding the critical resolved shear stress for BPD formation at the PVT growth temperature (2300–2400 °C) and

nucleate BPD loops and/or half loops at the growing crystal surface during PVT growth of 4H-SiC crystals.

Another important finding made in the X-ray topographs shown in Figures 1.3 and 1.4 is that the density of BPDs in the facet and near-facet regions of the as-grown crystal is significantly lower than the typical BPD densities in commercially available 4H-SiC substrates. The densities of BPDs in 4H-SiC substrates are typically 10^4–$10^5\,cm^{-2}$ [31, 32] and of the order of $10^3\,cm^{-2}$ for state-of-the-art 4H-SiC substrates [33]. By contrast, the estimated BPD density in the facet and near-facet regions of the crystal was less than $10^3\,cm^{-2}$. Sonoda et al. also examined two other 4H-SiC boules and found similar BPD densities in the crystal portion just beneath the facet and near-facet regions of the boules, although 4H-SiC substrates sliced out from the portions of the boules far from the growth front had typical BPD densities (10^4–$10^5\,cm^{-2}$) [27]. These results indicate that although BPDs could nucleate at the growing crystal surface, they hardly multiply in the facet and near-facet regions of PVT-grown 4H-SiC boules.

1.2.2 Cross-Sectional X-ray Topography Observations of Growth Front

To examine in more detail the BPD formation at the growth front, cross-sectional X-ray topography observations of PVT-grown 4H-SiC boules were performed [27]. The two portions in a vertically sliced wafer examined by transmission X-ray topography are illustrated schematically by open rectangles in Figure 1.1b. The solid-line rectangle corresponds to a portion right beneath the facet, whereas the dashed-line rectangle corresponds to a crystal portion near the shoulder region of the grown front.

Figure 1.5a shows a cross-sectional transmission X-ray topograph for the diffraction condition $\boldsymbol{g} = 11\bar{2}0$ of the portion right beneath the $(000\bar{1})$ facet, obtained by Sonoda et al. [27]. The topograph shows several dark vertical band and line contrasts, which correspond to low-angle boundaries and threading dislocations, respectively, penetrating the boule along the growth direction (*c*-axis). In addition to these vertical band and line contrasts, a number of horizontal line contrasts are also observed in the topograph. Figure 1.5b shows an enlarged topograph of the portion indicated by an open rectangle in Figure 1.5a. In Figure 1.5b, some of the horizontal line contrasts are marked by open triangles. The $\boldsymbol{g} \cdot \boldsymbol{b}$ contrast analysis revealed that these contrasts were caused by BPDs in the boule. Note here that a portion very close to the as-grown surface (facet), marked by a double-headed arrow in Figure 1.5b, is almost free of BPDs. This implies that BPDs hardly multiply in the facet and near-facet regions of the grown boule during PVT growth of 4H-SiC, which agrees well with the results of the plan-view X-ray topography observations shown in Figures 1.3 and 1.4.

Figure 1.5a also reveals that a number of BPDs exist in crystal portions distant from the growth front. This is consistent with the fact that 4H-SiC substrates prepared from these portions contain a high density of BPDs (10^4–$10^5\,cm^{-2}$). An important question here is where they came from. To clarify this point, a series of X-ray topographs (not shown) was taken from the center to the edge of the boule, and it was found that many BPDs extended continuously toward the edge of the

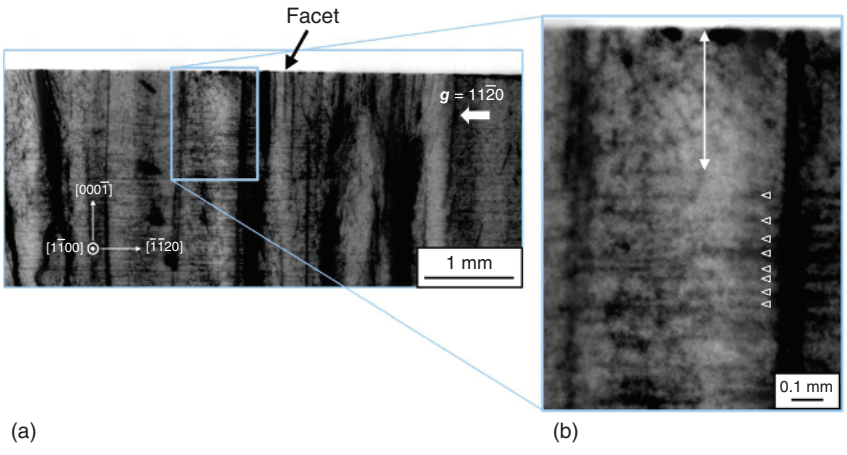

Figure 1.5 Cross-sectional X-ray topographs for diffraction condition $\boldsymbol{g} = 11\bar{2}0$ of a crystal portion right beneath the $(000\bar{1})$ facet of a PVT-grown 4H-SiC boule. (b) An enlarged topography image of the portion indicated by an open rectangle in (a). In (b), some of the horizontal line contrasts caused by BPDs are marked by open triangles. Source: Sonoda et al. [27].

boule and terminated at the shoulder region of the growth front. Figure 1.6 shows X-ray topographs of a crystal portion underneath the shoulder region of a 4H-SiC single-crystal boule [27]. The location of the crystal portion in the boule is indicated by a dashed-line rectangle in Figure 1.1b. Figure 1.6a,b shows X-ray topographs of the portion for the diffraction conditions $\boldsymbol{g} = 11\bar{2}0$ and $000\bar{8}$, respectively. As shown in Figure 1.6a ($11\bar{2}0$ topograph), a number of horizontal line contrasts extend along the basal plane; some of them are marked by open triangles in the figure. As shown in the figure, the horizontal line contrasts terminate at the as-grown surface of the boule. By contrast, they are lost in Figure 1.6b ($000\bar{8}$ topograph), and thus, they were ascribed to BPDs. To elaborate the BPD formation process, Sonoda et al. examined the other ends of these horizontal line contrasts and found that many of them terminated within the crystal at positions roughly below the facet. They observed a similar distribution of BPDs in the other half of the wafer and thus inferred that BPDs were nucleated at the shoulder region of the growth front and extended toward the inside of the grown boule via dislocation glide and multiplication processes during PVT growth. By contrast, such BPD glide and multiplication processes hardly occur in the facet and near-facet regions, resulting in a very low BPD density in the crystal portion right beneath these regions.

These BPD behaviors are illustrated more clearly in a wider-area transmission X-ray topograph shown in Figure 1.7, where the BPD-free crystal portion right beneath the facet and near-facet regions is bounded by a dashed line. In the figure, some of the BPDs extending along the basal plane in the grown crystal are indicated by open triangles. As shown in the figure, the boundary between the BPD-free portion and the other portions has a characteristic "round neck" shape that indicates that the BPD distribution in PVT-grown 4H-SiC crystals is controlled

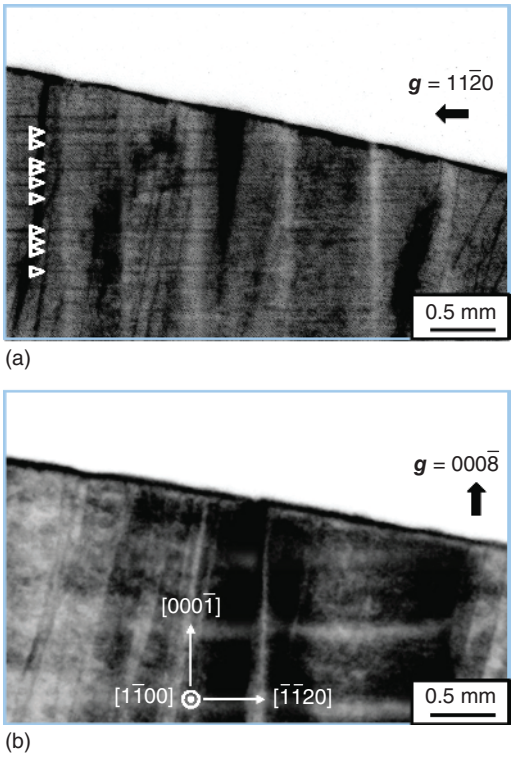

Figure 1.6 Cross-sectional X-ray topographs for diffraction conditions (a) $\boldsymbol{g} = 11\bar{2}0$ and (b) $000\bar{8}$ of a crystal portion underneath the shoulder region of the growth front of a PVT-grown 4H-SiC crystal, whose location in the crystal is indicated by a dashed line rectangle in Figure 1.1b. In (a), a number of horizontal line contrasts due to BPDs are observed; some of them are marked by open triangles. Source: Sonoda et al. [27].

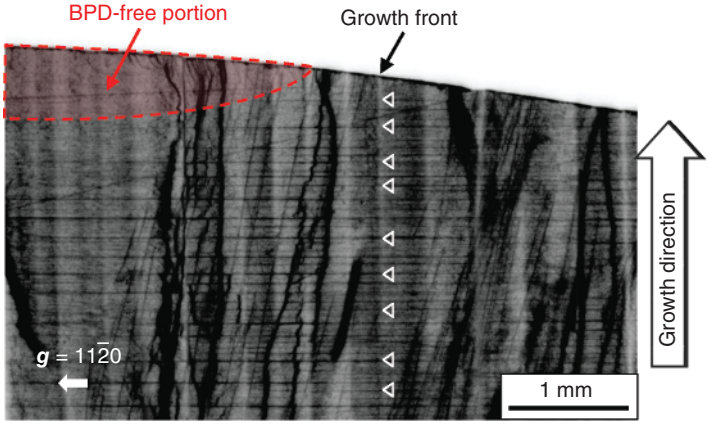

Figure 1.7 Wider-area transmission X-ray topograph for diffraction condition $\boldsymbol{g} = 11\bar{2}0$, which shows the existence of an almost BPD-free crystal portion right beneath the facet and near-facet regions at the growth front. Some of the BPDs extending along the basal plane are indicated by open triangles. The "round-neck" boundary between the BPD-free portion and the other portions is indicated by a dashed line.

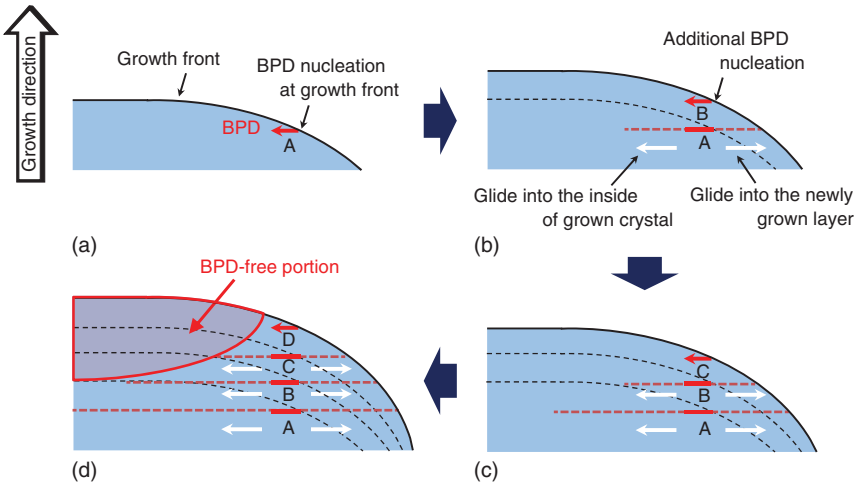

Figure 1.8 Schematics of temporal change of BPD distribution in a 4H-SiC crystal during PVT growth. (a) Nucleation of BPDs at the shoulder region of the grown crystal, and (b) glides of BPDs into the crystal and also toward the growth front of the crystal through the newly grown layer, together with the nucleation of additional BPDs at the growth front. (c) Repetition of processes (a, b) at the growth front of the newly grown layer during PVT growth, and (d) resulting round-neck distribution of BPDs due to the different glide distances of BPDs nucleated at different times in the PVT growth process.

by the BPD nucleation at the shoulder region of the grown crystal. This important conclusion was drawn by considering the glide and multiplication of BPDs after they nucleate at the shoulder region. These processes are illustrated in Figure 1.8, which shows schematically how the BPD distribution in a 4H-SiC crystal changes with time during PVT growth. Figure 1.8a shows the nucleation of BPDs at the shoulder region of a PVT-grown 4H-SiC crystal, and as the PVT growth proceeds, the nucleated BPDs glide into the grown crystal and also extend toward the growth front through the newly grown layer (Figure 1.8b). At this stage, additional BPDs nucleate at the growth front of the newly grown layer, and the aforementioned processes are repeated during PVT growth (Figure 1.8c), resulting in the round-neck distribution of BPDs (Figure 1.8d) because of the different glide distances of BPDs nucleated at different stages of the PVT growth process.

The BPD formation at the shoulder region of the PVT-grown SiC crystals coincides well with numerical results by Gao and Kakimoto [16]. They conducted three-dimensional numerical modeling of BPD multiplication in 4H-SiC bulk crystals. They calculated the resolved thermoelastic shear stresses on the basal plane during PVT growth of 4H-SiC and then substituted them into the Alexander–Hassen model to obtain the BPD distribution in PVT-grown 4H-SiC crystals. Their results showed that the shape of the growth front is key for BPD multiplication, with a largely convex growth front giving rise to a high resolved shear stress on the basal plane at the shoulder region of 4H-SiC boules during PVT growth, thus introducing many BPDs from the region. Their results also suggested that BPD multiplication occurs mainly in the crystal growth stage of the PVT growth process rather than in

the cooling stage. I believe that some irregularities at the growing crystal surface, such as TSD outcrops, become the nucleation sites of BPDs and lead to dislocation multiplication if a sufficiently high thermoelastic shear stress is imposed at these sites during PVT growth. The observed characteristic distribution of BPDs in the growth-front portion of 4H-SiC single-crystal boules corroborates this assumption.

1.2.3 Characteristic BPD Distribution in PVT-Grown 4H-SiC Crystals

In Section 1.2.2, it was revealed that many BPDs are introduced from the shoulder region of 4H-SiC crystals grown in the $[000\bar{1}]$ direction. However, it remains unclear how these BPDs behave in the crystals after their introduction. To clarify their behaviors, X-ray topography and Raman microscopy were conducted on a vertically sliced 4H-SiC $(11\bar{2}0)$ wafer, which is shown schematically in Figure 1.1b. Figure 1.9a,b shows transmission X-ray topographs of a 4H-SiC $(11\bar{2}0)$ wafer for the diffraction conditions $\boldsymbol{g} = 000\bar{8}$ and $1\bar{1}00$, respectively, obtained by Nakano et al. [26]. The area where the topographs were taken is indicated schematically by a red open square in Figure 1.9c. As shown in the topographs, strong horizontal line contrasts are observed in Figure 1.9b (diffraction vector: $1\bar{1}00$), which almost diminish in Figure 1.9a (diffraction vector: $000\bar{8}$). By contrast, in Figure 1.9a, line contrasts extending along the *c*-axis (growth direction) are observed, which correspond to TSDs. In Figure 1.9a, broad band contrasts are also observed at the positions where the strong horizontal line contrasts are observed in Figure 1.9b. The strong horizontal line contrasts observed in Figure 1.9b were caused by either BPDs or basal plane stacking faults in the crystal. To clarify the origin of the strong horizontal line contrasts observed in Figure 1.9b, Nakano et al. performed defect-selective etching

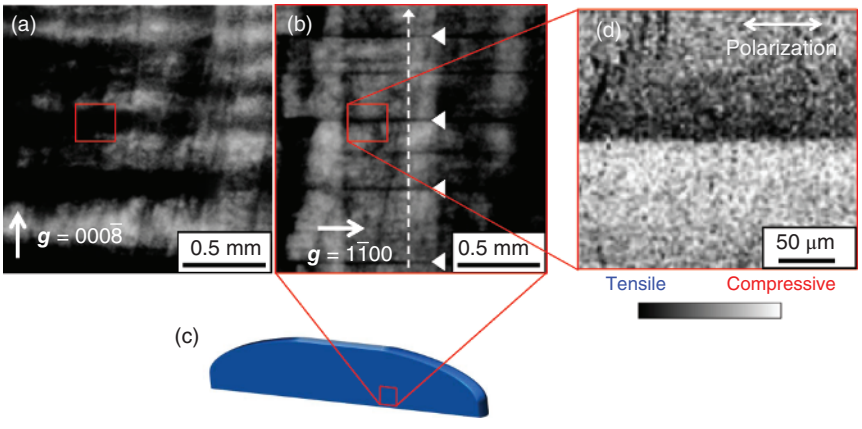

Figure 1.9 Transmission X-ray topographs for diffraction conditions (a) $\boldsymbol{g} = 000\bar{8}$ and (b) $1\bar{1}00$ of a vertically sliced 4H-SiC $(11\bar{2}0)$ wafer. In (c), the area in the wafer examined by transmission X-ray topography is shown as an open rectangle. (d) Raman microscopy image of a layer with a high density of BPDs (bunched BPDs). The white dashed arrow in (b) indicates the points and direction where the variations of the E_2 mode peak position and the *a*-lattice constant (Figure 1.10) were measured. Source: Nakano et al. [26]. © 2019, Elsevier.

(molten KOH etching) and found that they were caused by a high density of BPDs; Nakano et al. referred to this type of BPDs as "bunched BPDs" [26]. Note here that such bunched BPDs are arranged almost periodically along the growth direction in the grown crystal, as revealed in Figure 1.9b, where some of the bunched BPDs are indicated by closed white triangles.

To examine the structure of bunched BPDs in more detail, Raman microscopy imaging of bunched BPDs was conducted. The imaged area is indicated by a red open square in Figure 1.9a,b, and the peak position of the E_2 mode at ~776 cm^{-1} was plotted across this area with the polarization vectors of the incident and scattered light parallel to the basal plane. The obtained image is shown in Figure 1.9d, in which the light polarization is indicated by a double-headed arrow. As shown in the figure, there is a clear difference in the peak position between the upper and lower sides of bunched BPDs. In the upper side, the peak of the E_2 mode shifts to a lower position, while the peak is positioned at higher wavenumbers in the lower side, implying the existence of tensile (compressive) strain in the upper (lower) side of bunched BPDs.

Figure 1.10 shows how (i) the E_2 peak position and (ii) the a-lattice constant (lattice constant within the basal plane) vary in the growth direction as measured by high-resolution X-ray diffraction (HRXRD). These variations were measured along the line indicated by a white dashed arrow in Figure 1.9b. As shown in Figure 1.10a, the peak position shifted abruptly where bunched BPDs existed. The

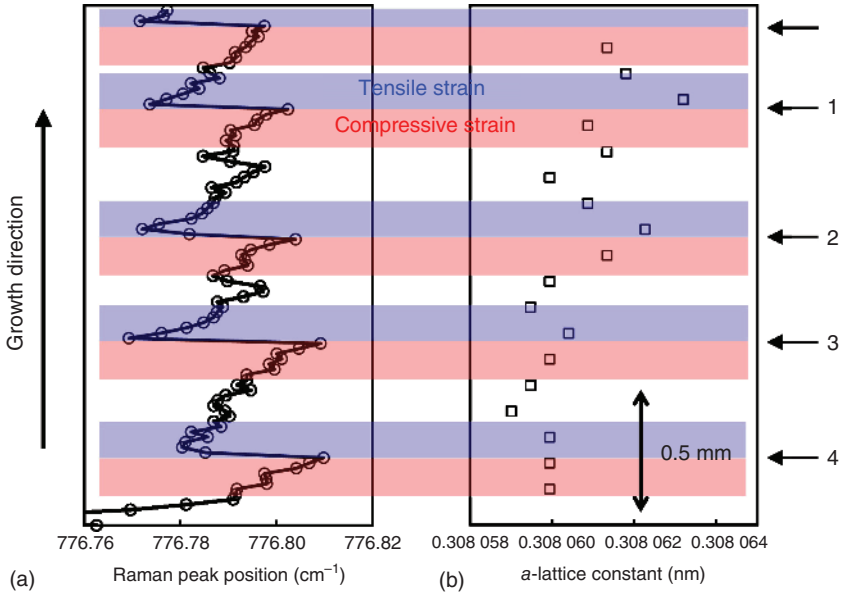

Figure 1.10 Variations of (a) peak position of Raman-active E_2 mode around 776 cm^{-1} and (b) the a-lattice constant measured using HRXRD in the growth direction on a vertically sliced 4H-SiC $(11\bar{2}0)$ wafer. The measured points and direction are indicated by a white dashed arrow in Figure 1.9b. (a) shows clearly that abrupt shifts of the E_2 peak position occurred at bunched BPDs; the positions of some of the bunched BPDs are indicated by arrows in the right-hand side of the figure (after [26]).

positions of some of the bunched BPDs are indicated by arrows in the right-hand side of Figure 1.10; those indicated by the arrows numbered from 1 to 4 correspond to the bunched BPDs indicated by closed white triangles in Figure 1.9b. The shift at bunched BPDs always occurred toward lower wavenumbers when the light beam was scanned from the bottom to the top of the grown crystal, implying that tensile strain within the basal plane always exists in the upper side of bunched BPDs [34–36]. The *a*-lattice constant also varied in the growth direction and increased in the upper side of bunched BPDs. This is consistent with the variation of the E_2 mode peak position, and it can be concluded that the tensile strain within the basal plane existing in the upper side of bunched BPDs resulted in a larger *a*-lattice constant.

The aforementioned results indicate that bunched BPDs are accompanied by extra half-planes pointing toward the seed crystal. This is reasonable if bunched BPDs are introduced by the thermoelastic stress imposed on the growing crystal during the PVT growth of SiC. The SiC PVT growth process is driven primarily by the temperature gradient along the *c*-axis (growth direction), and thus, a high σ_{rz} shear stress is imposed on the growing crystal during PVT growth, where *r* and *z* denote the radial and axial directions, respectively, of the grown crystal (*z* is parallel to the *c*-axis). At typical PVT growth temperatures (>2300 °C), SiC crystals deform plastically and the σ_{rz} shear stress is relieved considerably by the introduction of BPDs into the crystal. During the PVT growth process, a positive temperature gradient is maintained in the growth direction, and thus when the thermoelastic stress is relieved, BPDs are introduced that have extra half-planes pointing toward the seed crystal.

1.2.4 BPD Multiplication During PVT Growth

To investigate in more detail how BPDs behave during the PVT growth of 4H-SiC crystals, further extended Raman microscopy imaging of bunched BPDs in the lateral direction (parallel to the basal plane) was performed. The result of the Raman microscopy imaging is shown in Figure 1.11a. The image is a two-dimensional mapping of the peak position of the E_2 mode around 776 cm^{-1} on a vertically sliced 4H-SiC $(11\bar{2}0)$ wafer. Similarly to Figure 1.9d, the peak position differs clearly between the upper and lower sides of bunched BPDs. Note in this figure that the contrast difference between the upper and lower sides of bunched BPDs varies along the basal plane. In Figure 1.11a, portions with larger and smaller contrast differences are indicated by closed and open triangles, respectively. Nakano et al. found that the observed variation of the contrast difference (magnitude of the abrupt shift of the E_2 mode peak position at bunched BPDs) along the basal plane was correlated with the TSD density in the crystal [26]. Figure 1.11b shows the relationship between the contrast difference and the TSD density; the latter was estimated from the density of the line contrasts extending along the *c*-axis in X-ray topographs with the diffraction vector $\boldsymbol{g} = 000\bar{8}$ (e.g. Figure 1.9a) at the position where the contrast difference was measured by Raman microscopy. As shown in the figure, the magnitude of the abrupt peak shift at bunched BPDs is correlated well with TSD density: as the TSD density increases, the abrupt peak shift at bunched

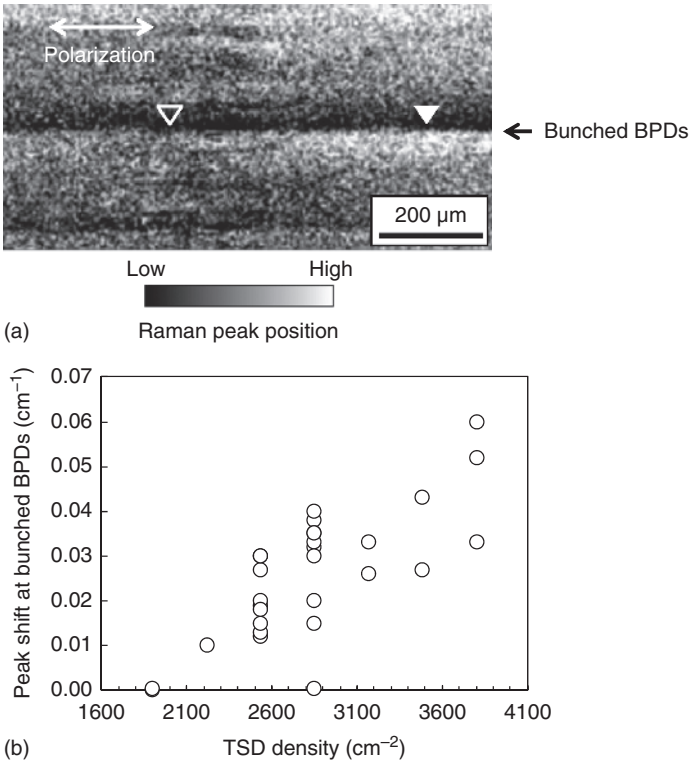

Figure 1.11 (a) Extended Raman microscopy image of bunched BPDs along the basal plane. The image shows variation of the E_2 mode peak position around bunched BPDs. The open and closed triangles in the image indicate portions that exhibited smaller and larger abrupt peak shifts, respectively, at the bunched BPDs. (b) A positive correlation between the magnitude of the abrupt peak shift at the bunched BPDs and the TSD density. Source: Nakano et al. [26]. © 2019, Elsevier.

BPDs becomes larger, which implies that the TSD and BPD densities in PVT-grown 4H-SiC crystals are correlated positively.

Ohtani et al. [37] reported a similar positive correlation between the TSD and BPD densities in PVT-grown 4H-SiC crystals. They conducted defect-selective etching using molten KOH to estimate the TSD and BPD densities in PVT-grown 4H-SiC crystals and found that the BPD density increased with the TSD density in the crystals. They ascribed this positive correlation to BPD multiplication around TSDs. Temperature gradients in 4H-SiC crystals during PVT growth cause BPDs to glide on the basal plane and cut through a forest of TSDs extending along the *c*-axis in the crystals. After crossing TSDs, BPDs have super jogs parallel to the *c*-axis, which are immobile and anchored in the crystal. When the BPDs glide further under thermoelastic stress during PVT growth and/or post-growth cooling, the well-known Frank–Read-type BPD multiplication occurs, and consequently the BPD density increases significantly around TSDs [32, 38]. This is why the BPD and TSD densities are correlated positively in 4H-SiC crystals.

As described in Section 1.2.3, BPDs have a characteristic distribution in the growth direction in PVT-grown 4H-SiC crystals; layers exist with a high density of BPDs (bunched BPDs) arranged almost periodically in the growth direction. As for the BPD formation in PVT-grown 4H-SiC crystals, it was also revealed in Section 1.2.2 that a number of BPDs are introduced from the shoulder region of the grown crystal during PVT growth. In this respect, it is noteworthy that bunched BPDs were observed relatively far from the shoulder region of the grown crystal. Given these results, an important question arises as to where and when bunched BPDs are introduced in crystals. A possible mechanism is that bunched BPDs are introduced from the side surfaces of grown crystals. The constant-diameter portion of a grown crystal has side surfaces that are located very close to the crucible inner walls, and under certain growth conditions, they can come into contact with the walls during PVT growth or cooling because of the different coefficients of thermal expansion of SiC and graphite. Therefore, the side surfaces of the grown crystal could be subject to high stress during PVT growth, thereby introducing a number of BPDs from the side surfaces. However, X-ray topography observations of a crystal portion near the side surfaces of 4H-SiC grown crystals revealed no bunched BPDs near the side surfaces [26].

To examine further the origin of bunched BPDs, further extended Raman microscopy analysis was performed in the growth direction. Figure 1.12 shows how the E_2 peak position varies in the growth direction [26]. The variations were measured along two lines, one that started from the bottom of a vertically sliced wafer and ended near the $(000\bar{1})$ facet region at the growth front (denoted by line A) and one that was close to the side surface (edge) of a grown crystal (denoted by line B). The locations of these two lines (lines A and B) in a vertically sliced $(11\bar{2}0)$ wafer are indicated schematically by dashed arrows in the inset of Figure 1.12. As shown in Figure 1.12, the E_2 peak position often shifted abruptly along line A;

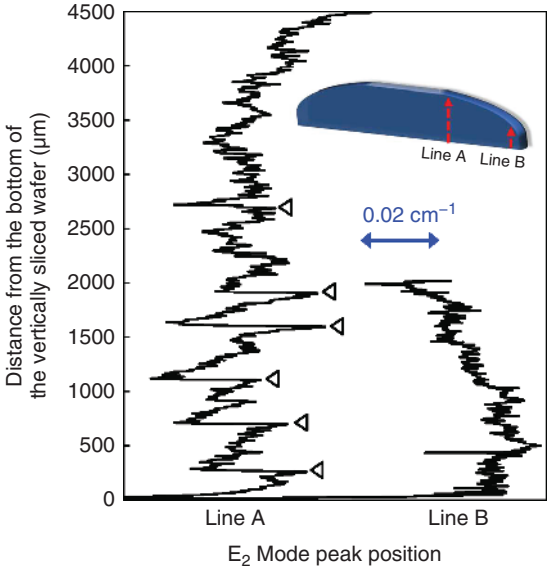

Figure 1.12 Variations of E_2 mode peak position in growth direction measured in the near-facet (line A) and edge (line B) portions of a vertically sliced 4H-SiC $(11\bar{2}0)$ wafer. The locations of the two measured portions (lines A and B) in the wafer are indicated by dashed arrows in the inset figure. Source: Nakano et al. [26]. © 2019, Elsevier.

some of the shifts are indicated by open triangles in the figure. By contrast, no such abrupt shifts were seen along line B. Note here that the abrupt shift intensified as the measured point approached the bottom of the vertically sliced wafer, implying that the BPD density in bunched BPDs increases gradually toward the seed crystal. Such an increase in BPD density toward the seed crystal is reasonable if bunched BPDs are introduced from the growth front (top surface of the growing crystal) during PVT growth. Once bunched BPDs are introduced from the growth front, their BPD density increases gradually as the growth proceeds, this being because the total duration of thermoelastic stress imposed on the growing crystal increases with the growth time.

The abovementioned discussions combine to give the important conclusion that bunched BPDs or their nuclei would be introduced at the growth front (domed surface) but hardly so from the side surfaces of grown crystals. The most plausible location where bunched BPDs are introduced would be the shoulder region of the growing crystal. Gao and Kakimoto [16] showed theoretically that the domed shape of the growth front gives rise to a high resolved shear stress on the basal plane in the shoulder region of the grown crystal during PVT growth of 4H-SiC, thus causing many BPDs to be introduced from that region. This theoretical prediction was subsequently confirmed experimentally by Sonoda et al. using X-ray topography [27]. The aforementioned results of Nakano et al. [26] indicate that the shoulder region of the growing crystal is a major source of BPDs, including bunched BPDs or their nuclei, and the BPDs introduced from that region would determine the distribution of BPDs throughout PVT-grown 4H-SiC crystals.

1.3 Dislocation Formation During Initial Stage of PVT Growth of 4H-SiC Crystals

1.3.1 Preparation of 4H-SiC Wafers with Beveled Interface Between Grown Crystal and Seed Crystal

In this section, I describe the formation of dislocations at the grown-crystal/seed interface of PVT-grown 4H-SiC crystals. As described in Section 1.1, most threading dislocations in PVT-grown 4H-SiC crystals form during the initial stage of PVT growth, and thus, it is essential to control the growth initiation to obtain high-quality 4H-SiC crystals. To reveal the processes for dislocation formation in the initial stage of 4H-SiC PVT growth, Shioura et al. [39] prepared 4H-SiC wafers containing a beveled interface between the grown crystal and the seed crystal and used them to examine the detailed distribution of crystallographic defects at and near the interface. Figure 1.13 shows schematics of the slicing geometry of a 4H-SiC crystal grown on a 4° off-oriented $(000\bar{1})$ seed crystal, providing a 1.5° off-oriented $(000\bar{1})$ wafer, which has a beveled interface between the grown crystal and seed crystal [39]. Figure 1.13a is a schematic side view of a nitrogen-doped 4H-SiC crystal grown on a 4° off-oriented $(000\bar{1})$ seed crystal and a slightly off-oriented (1.5° off-oriented approximately toward $[11\bar{2}0]$) $(000\bar{1})$ wafer sliced out from the grown crystal, while

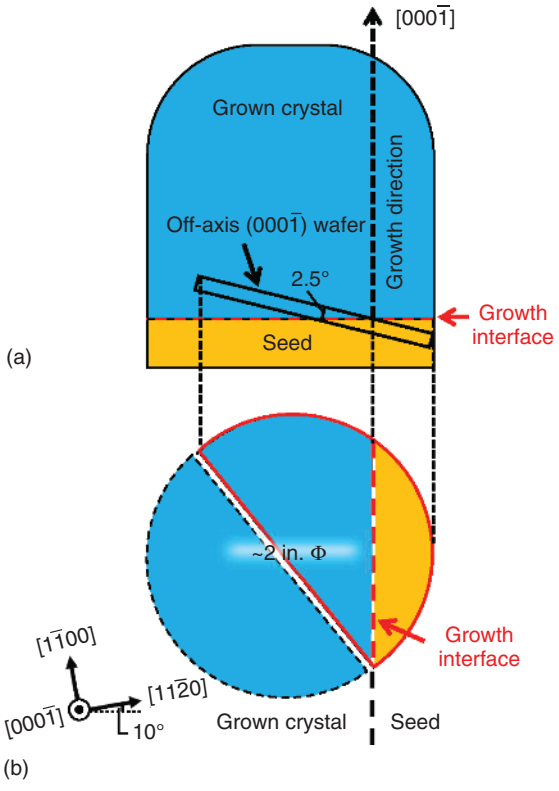

Figure 1.13 Schematics of slicing geometry of a nitrogen-doped 4H-SiC crystal grown on a 4° off-oriented (000$\bar{1}$) seed crystal, providing a 1.5° off-oriented (000$\bar{1}$) wafer, which has a beveled interface between the grown crystal and the seed crystal. (a) Side view of grown crystal and 1.5° off-oriented (000$\bar{1}$) wafer sliced out from the crystal. (b) Top view of sliced wafer. Source: Shioura et al. [39]. © 2019, Elsevier.

Figure 1.13b shows a top view of the sliced wafer. The angle between the wafer surface and the grown-crystal/seed interface was relatively shallow (2.5°), and thus, the defective near-interface region was substantially enlarged to facilitate detailed observations and analyses of defects at and near the interface. Shioura et al. examined this substantially enlarged interfacial region between the grown crystal and seed crystal using Raman microscopy and X-ray topography, and on the basis of the obtained results elucidated the formation mechanisms of crystallographic defects during the initial stage of PVT growth of 4H-SiC crystals [39].

1.3.2 Determination of Grown-Crystal/Seed Interface by Raman Microscopy

Figure 1.14 shows (a) an intensity mapping image of the whole 1.5° off-oriented 4H-SiC (000$\bar{1}$) wafer containing the grown-crystal/seed interface, acquired using the intensity of the longitudinal optical phonon–plasmon-coupled (LOPC) mode around 983 cm^{-1}, and (b) a reflection X-ray topograph of the wafer for the diffraction condition $\boldsymbol{g} = 11\bar{2}\bar{8}$ [39]. The intensity of the LOPC mode is known to be very sensitive to the carrier (electron) concentration in 4H-SiC crystals: as the electron concentration increases, the intensity decreases rapidly [40, 41]. As shown in Figure 1.14a, the LOPC mode scattering intensity differs markedly between the seed

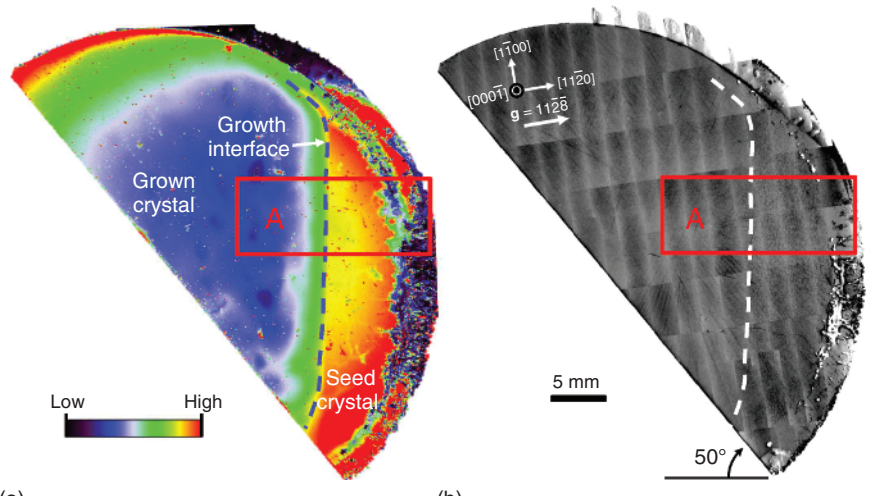

Figure 1.14 (a) Raman mapping image using longitudinal optical phonon–plasmon-coupled (LOPC) mode intensity of a 1.5° off-oriented 4H-SiC (000$\bar{1}$) wafer with a beveled interface between the grown crystal and the seed crystal, which corresponds to the upper right part of the wafer illustrated schematically in Figure 1.13b. (b) Reflection X-ray topograph of the 1.5° off-oriented 4H-SiC (000$\bar{1}$) wafer in the diffraction condition $\boldsymbol{g} = 11\bar{2}\bar{8}$. The position of the interface between the grown crystal and seed crystal is indicated by a dashed line, and the region used for subsequent Raman microscopy and X-ray topography analyses is indicated by a red open rectangle (region A) in both (a, b). Source: Shioura et al. [39]. © 2019, Elsevier.

and grown crystal regions, and thus, their interface can be determined by Raman microscopy. Figure 1.15 shows enlarged Raman microscopy images across region A in the wafer, whose location is indicated by a red open rectangle in Figure 1.14a,b. In Figure 1.15, mapping images of (a) Raman scattering intensity, (b) peak position, and (c) width of the LOPC asymmetric peak are shown, together with their line profiles across the grown-crystal/seed interface, namely, (d) intensity, (e) peak position, and (f) peak width. As shown in Figure 1.15d, the Raman scattering intensity decreases rapidly from the point indicated by a red triangle in the figure toward the left-hand side of the figure (in the growth direction). Ohshige et al. reported that the electron concentration in PVT-grown 4H-SiC crystals increases abruptly at the grown-crystal/seed interface because of the enrichment of nitrogen donors in the crystal in its initial growth stage [23]. The rapid decrease in the scattering intensity shown in Figure 1.15d is thought to be due to the nitrogen enrichment at the grown-crystal/seed interface, and thus, using the LOPC intensity profile, the location of the interface between the grown crystal and the seed crystal can be determined reasonably as the point indicated by a red triangle in Figure 1.15d.

According to the scheme described earlier, the grown-crystal/seed interface was determined and indicated as a dashed line in Figures 1.14 and 1.15a–c [39]. In all the figures, the left-hand side of the dashed line is the grown crystal, while the right-hand side corresponds to the seed crystal.

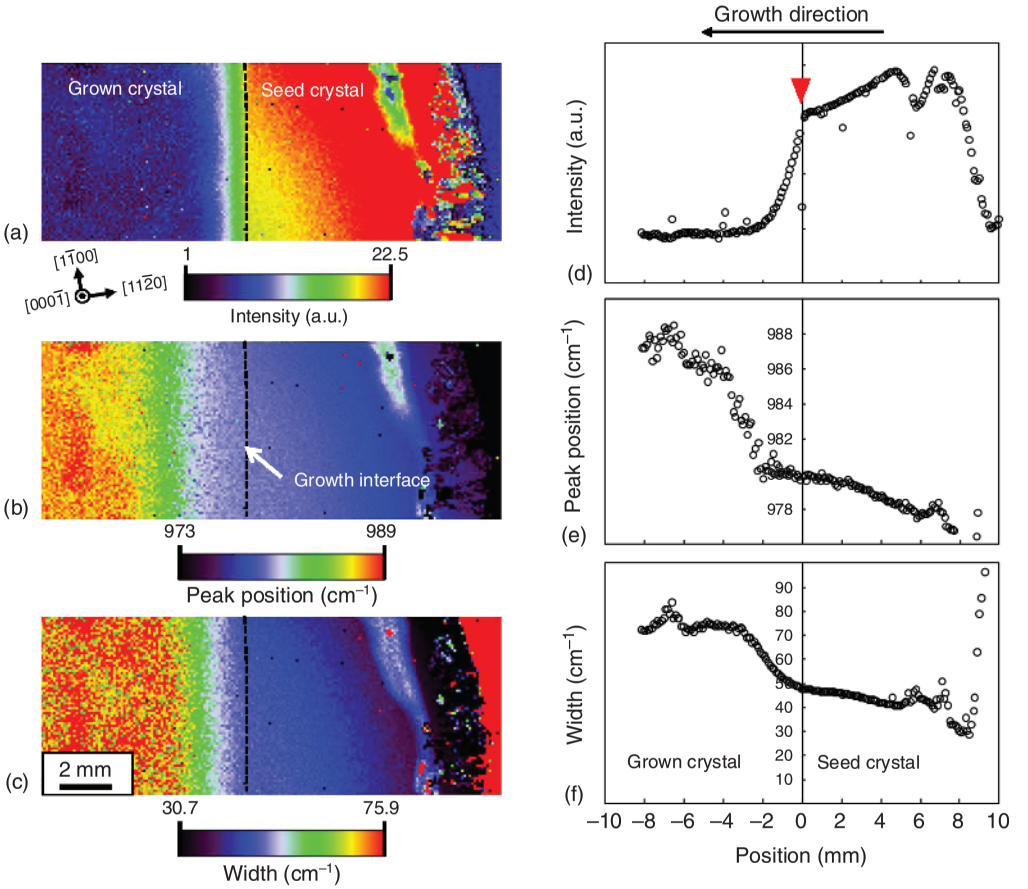

Figure 1.15 Raman microscopy images of region A, which is indicated by a red open rectangle in Figure 1.14: (a) scattering intensity, (b) peak position, and (c) width of the asymmetric LOPC peak around 983 cm^{-1}, where the position of the grown-crystal/seed interface is indicated by a dashed line in each image. The variations of the intensity, peak position, and width of the LOPC peak across the interface are shown in (d–f), respectively, where the data were averaged in the direction parallel to the grown-crystal/seed interface (after [39]). Source: Shioura et al.

1.3.3 X-ray Topography Observations of Dislocation Structure at Grown-Crystal/Seed Interface

To examine more clearly the defect structure near the grown-crystal/seed interface, an enlarged X-ray topograph from the interface region was taken and is shown in Figure 1.16 [39], which is a reflection X-ray topography image for the diffraction condition $\boldsymbol{g} = 11\bar{2}\bar{8}$ acquired from region A indicated by a red open rectangle in Figure 1.14. The grown-crystal/seed interface determined by Raman microscopy imaging is indicated by a dashed line in Figure 1.16. The image shows the existence of widespread networks of BPDs near the grown-crystal/seed interface; some of them are marked by white triangles in Figure 1.16. Similar BPD networks have been reported by Tani et al. [24]. They conducted high-voltage transmission electron microscopy (HVTEM) observations and found that BPDs in the networks connected to each other to form cell-like structures and decomposed into stacking faults at the triple nodes of the networks. In Figure 1.16, a cell-like feature of the BPD networks formed at the grown-crystal/seed interface is also observed, and more interestingly, it was found that the networks extended considerably into the seed crystal.

Shioura et al. conducted $\boldsymbol{g} \cdot \boldsymbol{b}$ contrast analyses of the BPD networks observed at the grown-crystal/seed interface to determine the nature of the networks [39]. The results are shown in Figure 1.17, where reflection X-ray topographs of region B, which is indicated by an open square in Figure 1.16, are shown; they were taken for the diffraction conditions (a) $\boldsymbol{g} = 11\bar{2}\bar{8}$, (b) $\bar{1}01\bar{7}$, (c) $\bar{1}10\bar{7}$, and (d) $01\bar{1}\bar{7}$. Figure 1.17 reveals that under each diffraction condition, some parts of the BPD networks become out of contrast; the parts that are out of contrast under each diffraction condition are indicated by white lines in each topograph. The extinction of the diffraction contrast means that the Burgers vectors associated with these parts of the BPD networks are perpendicular to the diffraction vector, and thus, the results of the $\boldsymbol{g} \cdot \boldsymbol{b}$ contrast analyses shown in Figure 1.17 demonstrate that the BPD networks

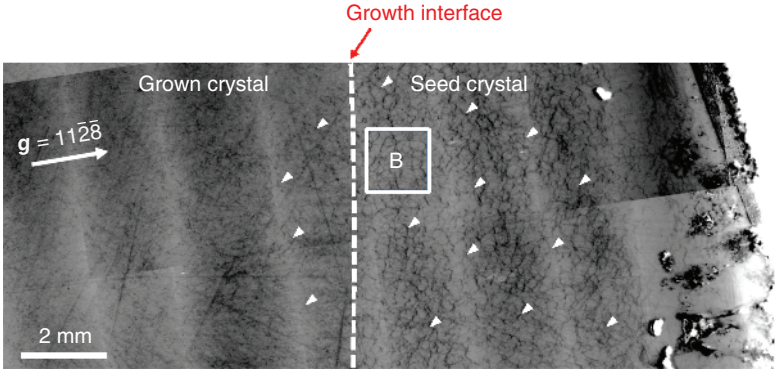

Figure 1.16 Reflection X-ray topograph for diffraction condition $\boldsymbol{g} = 11\bar{2}\bar{8}$ of region A in 1.5° off-oriented 4H-SiC (000$\bar{1}$) wafer, where the position of the grown-crystal/seed interface is indicated by a white dashed line. In this figure, the region used for subsequent $\boldsymbol{g} \cdot \boldsymbol{b}$ analyses (see Figure 1.17) is indicated by a white open square (region B). Source: Shioura et al. [39].

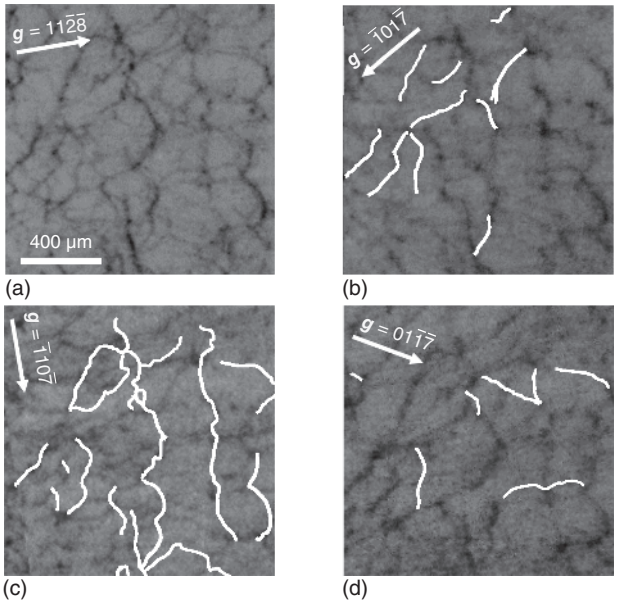

Figure 1.17 Reflection X-ray topographs of BPD networks observed in region B of 1.5° off-oriented 4H-SiC (0001) wafer for diffraction conditions (a) $\boldsymbol{g} = 11\bar{2}\bar{8}$, (b) $\bar{1}01\bar{7}$, (c) $\bar{1}10\bar{7}$, and (d) $01\bar{1}\bar{7}$. The diminished parts of the BPD networks under each diffraction condition are indicated by white solid lines in each topograph. Source: Shioura et al. [39].

consist mainly of edge-type BPDs that have a Burgers vector perpendicular to the dislocation line. This result suggests that a high density of BPDs observed at the grown-crystal/seed interface would have been caused by some form of misfit stress within the basal plane imposed at the interface during the initial stage of PVT growth.

To investigate further the nature of the BPD networks, the bending of the (0001) basal plane was examined by means of measurements of the peak position shift of the ω-scan 0008 HRXRD rocking curve across the grown-crystal/seed interface [39]. The results indicated that the (0001) basal plane in the slightly off-oriented $(000\bar{1})$ wafer contained the beveled interface between the grown crystal and seed crystal bent in a concave manner in the $[000\bar{1}]$ growth direction, which implies that the crystal near the grown-crystal/seed interface contained extra half-planes pointing in the [0001] direction (the backside of the seed crystal).

1.3.4 Formation Mechanism of BPD Networks and Their Migration into Seed Crystal

It was revealed by HRXRD measurements that there were extra half-planes pointing in the [0001] direction in the crystal near the grown-crystal/seed interface [39]. These extra half-planes are thought to be associated with the BPD networks existing near the grown-crystal/seed interface. It was also revealed that most parts of BPDs comprising the networks have an edge component, and thus, they are likely to have

been caused by misfit strain accommodated at the interface during the initial stage of SiC PVT growth.

The misfit strain within the basal plane at the grown-crystal/seed interface has two possible origins, namely, (i) nitrogen enrichment at the interface and (ii) the temperature gradient in the growth direction imposed on the growing crystal in the initial stage of PVT growth. The nitrogen enrichment at the grown-crystal/seed interface has been reported by several authors [12, 22–25]. The grown crystal was doped intentionally with nitrogen in the same concentration as the seed crystal; however, residual nitrogen impurities in the growth atmosphere and/or those adsorbed on the source powder surface could give rise to a relative enrichment of nitrogen in the crystal grown during the early stage of PVT growth. Nitrogen doping has been reported to give rise to a smaller lattice spacing [42] and also a smaller coefficient of thermal expansion [43] within the basal plane for 4H-SiC crystals; thus, a higher nitrogen concentration in the grown crystal than that of the underlying seed crystal would give rise to misfit strain between the grown crystal and the seed. However, in this case, the sign of the misfit strain is opposite to that having caused the BPD networks; the nitrogen enrichment in the grown crystal results in a smaller lattice constant within the basal plane at the PVT growth temperature (~2300 °C), yielding BPDs with extra half-planes pointing in the growth direction when the misfit strain is relieved. This is contradictory to the result of the HRXRD measurements.

Another possible origin of the misfit strain at the grown-crystal/seed interface is the temperature gradient at the interface. Usually, during SiC PVT growth, a positive temperature gradient in the growth direction is set in the growth zone by placing the growth crucible asymmetrically in the radio-frequency (RF) induction coil or the heating furnace (see Figures 1.1a and 1.18a). In addition to this intentionally imposed temperature gradient, the latent heat dissipation associated with the condensation of Si- and C-bearing species sublimed from the source powder would result in an enhanced positive temperature gradient during PVT growth. In this respect, note that SiC has an extremely large latent heat of phase transition from the vapor to the solid (heat of condensation/sublimation), which is estimated to be 580 kJ/mol [44] and more than 10 times larger than that of Si solidification from the melt (50.6 kJ/mol) [45].

With respect to the heating due to the latent heat, another important factor that should be considered is the thickness of the grown crystal in the initial stage of growth. Figure 1.18 explains schematically how the thickness of the grown crystal affects the dissipation of latent heat. Upon condensation of the Si- and C-bearing species, the latent heat is released on the growing crystal surface. The seed crystal is usually placed on a graphite holder, which has a much lower thermal conductivity than that of 4H-SiC at the PVT growth temperature. In the initial stage of PVT growth, the SiC crystal (seed crystal plus grown crystal) is very thin, and thus, all the heat generated by the condensation of Si- and C-bearing species must be dissipated through the backside of the seed crystal (Figure 1.18d). However, the low thermal conductivity of the graphite seed holder means that the generated heat is not dissipated efficiently, and thus, an even larger positive temperature gradient is established at the growing crystal surface during the initial stage of PVT

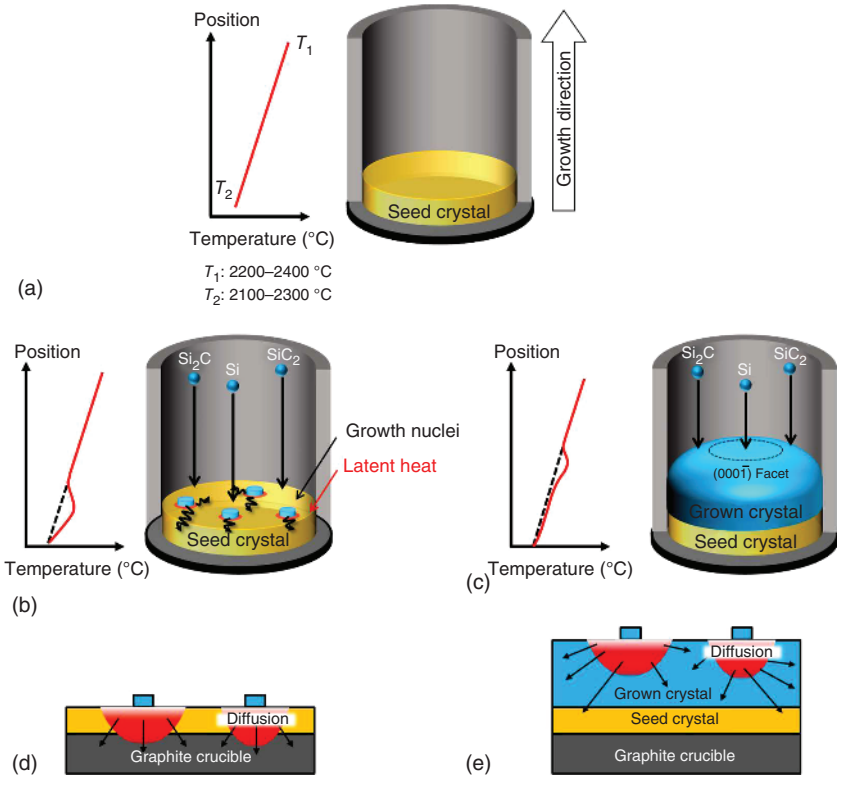

Figure 1.18 Schematics of latent heat dissipation during PVT growth of 4H-SiC crystals. (a) Positive temperature gradient in the growth direction imposed intentionally in the growth crucible by placing it asymmetrically in the RF induction coil or the heating furnace. (b) Enhancement of temperature gradient at growth front of the grown crystal caused by the poor latent heat dissipation in the initial stage of PVT growth because of the low thermal conductivity of the graphite seed holder; this effect is shown schematically in (d). (c) Case of a thick grown crystal after sufficient time of crystal growth; the enhanced temperature gradient at the growth front is lessened considerably because the generated latent heat can be dissipated efficiently through the thickly grown SiC crystal, as shown schematically in (e).

growth (Figure 1.18b). This large positive temperature gradient causes a large misfit strain within the basal plane at and near the grown-crystal/seed interface, which is relieved by the introduction of BPDs during growth. By contrast, as the grown crystal becomes thicker as it grows, the latent heat is dissipated more efficiently through the body of the thick grown crystal (Figure 1.18e). This lessens considerably the enhanced temperature gradient at the growth front due to the condensation of the Si- and C-bearing species (Figure 1.18c).

The aforementioned strain generation and relaxation processes due to the latent heat are illustrated schematically in Figure 1.19. The figure depicts sequentially (a) the seed crystal prior to PVT growth, (b) the basal plane bending associated with the large temperature gradient in the initial stage of growth, which occurs in a convex manner in the growth direction, (c) the introduction of BPDs to relieve the

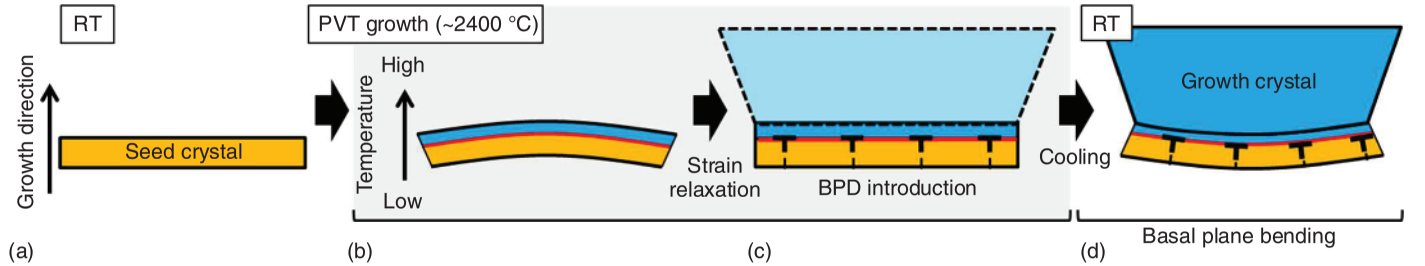

Figure 1.19 Schematic of introduction of BPDs at grown-crystal/seed interface during PVT growth process, and the resulting basal plane bending after the growth process. Source: Shioura et al. [39]. © 2019, Elsevier; (a) seed crystal prior to PVT growth, (b) basal plane bending associated the large temperature gradient at the initial stage of growth, which occurs in a convex manner toward the growth direction, (c) introduction of BPDs to relax the misfit strain within the basal plane at the grown-crystal/seed interface, and (d) concave-shape basal plane bending toward the growth direction after cooling to room temperature.

misfit strain within the basal plane at the grown-crystal/seed interface, and (d) the resultant concave-shaped basal plane bending in the growth direction after PVT growth. The large basal plane bending due to the poor heat dissipation in the initial stage of PVT growth of SiC was observed experimentally by Hock et al. using in situ X-ray diffraction [46]. They found that the degree of basal plane bending increased with the growth rate, implying that the latent heating due to the condensation of source gas species plays an important role in the basal plane bending in the initial stage of PVT growth.

The final concave shape of the basal plane in the growth direction shown in Figure 1.19d is consistent with the lattice bending observed by HRXRD, and thus, the large positive temperature gradient established at the growing crystal surface during the initial stage of PVT growth would be the most plausible cause of the observed BPD networks. The relationship between the observed BPD networks and the formation of threading dislocations in the initial stage of PVT growth [10–12] is yet to be clarified. However, in Figure 1.17, in addition to the BPD networks, dot-like features are also observed at the nodes of the BPD networks. They are likely to correspond to threading dislocations and suggest that the BPD networks are related closely to them and would be an important source of threading dislocations in PVT-grown 4H-SiC crystals.

As revealed in Figure 1.16, the BPD networks extended fairly deeply in the seed crystal. The maximum depth of the networks in the seed crystal can be estimated from their positions on the surface of the 1.5° off-oriented $(000\bar{1})$ wafer; the networks extended up to 7 mm on the wafer surface from the grown-crystal/seed interface toward the backside of the seed crystal. The distance of 7 mm on the wafer surface corresponds to a depth of 300 μm from the grown-crystal/seed interface toward the backside of the seed crystal. In the initial stage of PVT growth, growth islands are likely to nucleate on the seed crystal surface and then coalesce as the crystal growth proceeds (see Figure 1.18b). Under a large positive temperature gradient, the growth islands tend to incorporate BPDs to relieve the misfit strain due to the temperature gradient, and when the islands coalesce, the BPDs are rearranged and form networks at the grown-crystal/seed interface. The results obtained by Shioura et al. indicated that these BPD networks at the interface were accompanied by extra half-planes pointing toward the backside of the seed crystal and caused the (0001) basal plane to bend in a concave manner in the growth direction after the PVT growth process [39]. An important question here is how and why these BPD networks migrated into the seed crystal during PVT growth.

There are two possible mechanisms for the migration of the BPD networks into the seed crystal, namely, (i) the glide motion of BPDs on the basal plane and (ii) the climb motion of BPDs across the basal plane. To clarify the mechanism for BPD migration into the seed crystal during PVT growth, Shioura et al. conducted a masked PVT growth experiment on a 4° off-oriented $(000\bar{1})$ seed crystal [39]. The result is shown in Figure 1.20, where a reflection X-ray topograph for the diffraction condition $\boldsymbol{g} = 11\bar{2}\bar{8}$ acquired from the boundary area between the masked and unmasked regions of the seed crystal is shown. The masked region (right-hand side of the figure) was covered with a graphite plate during PVT growth to prevent

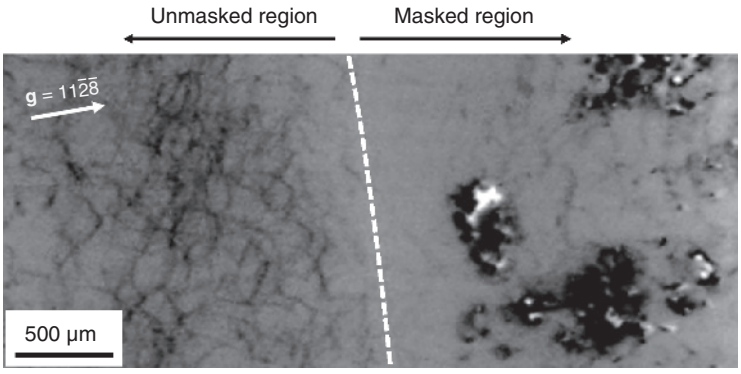

Figure 1.20 Enlarged reflection X-ray topograph for diffraction condition $\boldsymbol{g} = 11\bar{2}\bar{8}$ acquired from the boundary area between the masked and unmasked regions of the seed crystal; the 4H-SiC crystal was grown on the unmasked region (left-hand side of the dashed line in the topograph), whereas no crystal growth occurred on the masked region (right-hand side of the dashed line). The topograph shows clearly that the BPD networks in the seed crystal existed only in the unmasked region of the seed crystal. Source: Shioura et al. [39].

crystal growth. As shown in the figure, BPD networks exist only in the unmasked region and do not extend into the masked region. This result shows clearly that the observed BPD networks migrated into the seed crystal through the climb motion of dislocations, as schematically illustrated in Figure 1.21, rather than the glide motion. This is because, had the glide motion been the dominant mechanism for BPD migration, then the BPD networks formed during the initial stage of PVT growth should have glided on the basal plane into the masked region beyond the boundary between the unmasked and masked regions and then been observed in the masked region of the seed crystal after the crystal growth.

The climb motion of dislocations is driven by the injection, diffusion, and incorporation of intrinsic point defects, such as vacancies and interstitials, to the dislocations [47]. As described in Section 1.3.3, the observed BPD networks were accompanied by extra half-planes pointing toward the backside of the seed crystal, and thus, their migration toward the backside of the seed crystal requires vacancies to be incorporated in the dislocations as illustrated schematically in Figure 1.20. Given the migration depth of the BPD networks, it is clear that a large number of vacancies were injected during the initial stage of PVT growth. The mechanism for this remains unclear, but the poor dissipation of the latent heat in the initial stage of PVT growth (see Figure 1.18b,d) would cause local heating of the growing crystal surface, which may induce the injection of a large number of vacancies into the growing crystal.

1.4 Conclusions

SiC is a promising material for the next generation of power semiconductor devices, and the adoption of SiC power devices is critical for enabling faster, smaller, lighter,

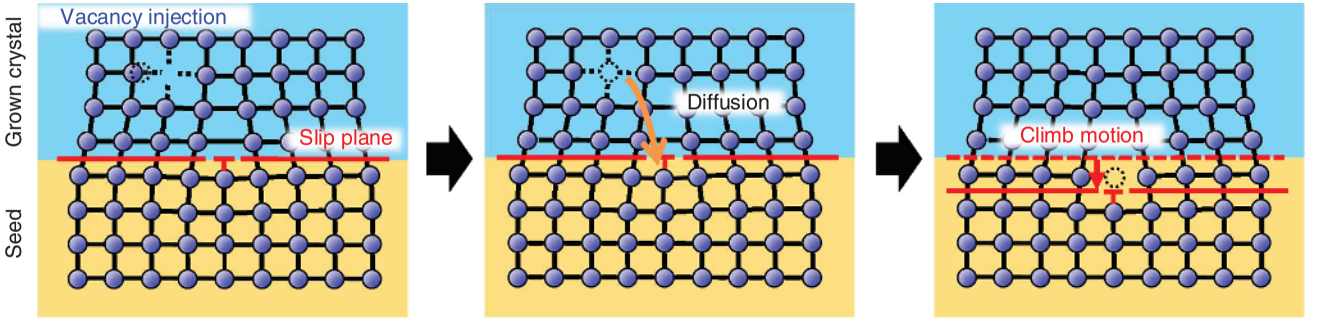

Figure 1.21 Schematic of the climb motion of a BPD toward the backside of the seed crystal due to the vacancy injection into the growing crystal during PVT growth. Source: Shioura et al. [39]. © 2019, Elsevier.

and more powerful power electronic systems. However, it is amply clear that such a successful adoption of SiC power devices for a wide range of power electronics systems relies considerably on establishing the manufacturing technology for large-diameter high-quality SiC single crystals. This chapter described recent progress in understanding the dislocation formation processes in PVT-grown SiC crystals, which is essential for obtaining high-quality SiC crystals.

After a brief introduction (Section 1.1), Section 1.2 was dedicated to understanding the BPD nucleation and multiplication processes during the PVT growth of 4H-SiC crystals. A large number of BPDs are introduced from the shoulder region of the growth front of 4H-SiC crystals, where a large thermoelastic shear stress is thought to be imposed during PVT growth. Detailed investigations of the BPD distribution in grown crystals suggest that BPDs nucleated at the shoulder region of a growing crystal largely determine the BPD distribution across the entire crystal.

In Section 1.3, the defect structure at the grown-crystal/seed interface of PVT-grown 4H-SiC crystals was investigated using 4H-SiC wafers with a beveled interface between the grown crystal and seed crystal. The existence of BPD networks at the grown-crystal/seed interface was revealed, and they extended considerably into the seed crystal. Such networks were likely to be caused by a large positive temperature gradient imposed on the growing crystal surface because of the local heating by the latent heat dissipation associated with the condensation of Si- and C-bearing species from the vapor during the initial stage of PVT growth. It was also revealed by masked-growth experiments that the migration of the BPD networks deep into the seed crystal was caused by the injection of a large number of vacancies during the initial stage of PVT growth of 4H-SiC crystals.

References

1 Kimoto, T. and Cooper, J.A. (2014). *Fundamentals of Silicon Carbide Technology: Growth, Characterization, Devices, and Applications*. Singapore: Wiley.
2 Tairov, Yu.M. and Tsvetkov, V.F. (1978). *J. Cryst. Growth* 43: 209.
3 Wahab, Q., Ellison, A., Henry, A. et al. (2000). *Appl. Phys. Lett.* 76: 2725.
4 Fujiwara, H., Naruoka, H., Konishi, M. et al. (2012). *Appl. Phys. Lett.* 100: 242102.
5 Yamamoto, K., Nagaya, M., Watanabe, H. et al. (2012). *Mater. Sci. Forum* 717–720: 477.
6 Agarwal, A., Fatima, H., Haney, S., and Sei-Hyung, R. (2007). *IEEE Electron Device Lett.* 28: 587.
7 Veliadis, V., Hearne, H., Stewart, E.J. et al. (2012). *IEEE Electron Device Lett.* 33: 952.
8 Bergman, P., Lendenmann, H., Nilsson, P.A. et al. (2001). *Mater. Sci. Forum* 353–356: 299.
9 Lendenmann, H., Dahquist, F., Johansson, N. et al. (2001). *Mater. Sci. Forum* 353–356: 727.
10 Takahashi, J., Ohtani, N., and Kanaya, M. (1996). *J. Cryst. Growth* 167: 596.

11 Sanchez, E.K., Liu, J.Q., De Graef, M. et al. (2002). *J. Appl. Phys.* 91: 1143.
12 Suo, H., Tsukimoto, S., Eto, K. et al. (2018). *Jpn. J. Appl. Phys.* 57: 065501.
13 Hobgood, H.McD, Brady, M.F., Brixius, W.H. et al. (2000). *Mater. Sci. Forum* 338–342: 3.
14 Selder, M., Kadinski, L., Durst, F., and Hofmann, D. (2001). *J. Cryst. Growth* 226: 501.
15 Ma, R.-H., Zhang, H., Dudley, M., and Prasad, V. (2003). *J. Cryst. Growth* 258: 318.
16 Gao, B. and Kakimoto, T. (2014). *Cryst. Growth Des.* 14: 1272.
17 Herro, Z.G., Epelbaum, B.M., Bickermann, M. et al. (2004). *J. Cryst. Growth* 262: 105.
18 Yamaguchi, T., Ohtomo, K., Sato, S. et al. (2015). *J. Cryst. Growth* 431: 24.
19 Pons, M., Madar, R., and Billon, T. (2003). *Silicon Carbide – Recent Major Advances* (eds. W.J. Choyke, H. Matsunami and G. Pensl), 121–136. Berlin: Springer.
20 Powell, A.R., Leonard, R.T., Brady, M.F. et al. (2004). *Mater. Sci. Forum* 457–460: 41.
21 Tymicki, E., Grasza, K., Diduszko, R. et al. (2007). *Cryst. Res. Technol.* 42: 1232.
22 Ohtani, N., Ohshige, C., Katsuno, M. et al. (2014). *J. Cryst. Growth* 386: 9.
23 Ohshige, C., Takahashi, T., Ohtani, N. et al. (2014). *J. Cryst. Growth* 408: 1.
24 Tani, K., Fujimoto, T., Kamei, K. et al. (2016). *Mater. Sci. Forum* 858: 73.
25 Straubinger, T.L., Bickermann, M., Weingärtner, R. et al. (2002). *J. Cryst. Growth* 240: 117.
26 Nakano, T., Shinagawa, N., Yabu, M., and Ohtani, N. (2019). *J. Cryst. Growth* 516: 51.
27 Sonoda, M., Nakano, T., Shioura, K. et al. (2018). *J. Cryst. Growth* 499: 24.
28 Wang, S., Dudley, M., Carter, C. Jr., et al. (1993). *Mater. Res. Soc. Symp. Proc.* 307: 249.
29 Zhang, X., Ha, S., Hanlumnyang, Y. et al. (2007). *J. Appl. Phys.* 101: 053517.
30 Hirth, J.P. and Lothe, J. (1982). *Theory of Dislocations*, 2e, 63. New York: Wiley.
31 Ha, S., Mieszkowski, M., Skowronski, M., and Rowland, L.B. (2002). *J. Cryst. Growth* 244: 257.
32 Ohtani, N., Katsuno, M., Tsuge, H. et al. (2006). *Jpn. J. Appl. Phys.* 45: 1738.
33 Powell, A.R., Sumakeris, J.J., Khlebnikov, Y. et al. (2016). *Mater. Sci. Forum* 858: 5.
34 Nakashima, S. and Harima, H. (1997). *Phys. Status Solidi A* 162: 39.
35 Sugie, R. and Uchida, T. (2017). *J. Appl. Phys.* 122: 195703.
36 Sakakima, H., Takamoto, S., Murakami, Y. et al. (2018). *Jpn. J. Appl. Phys.* 57: 106602.
37 Ohtani, N., Katsuno, M., Fujimoto, T. et al. (2009). *Jpn. J. Appl. Phys.* 48: 065503.
38 Chen, Y., Dhanaraj, G., Dudley, M. et al. (2006). *Mater. Res. Soc. Symp. Proc.* 911: 151.
39 Shioura, K., Shinagawa, N., Izawa, T., and Ohtani, N. (2019). *J. Cryst. Growth* 515: 58.
40 Yugami, H., Nakashima, S., Mitsuishi, A. et al. (1987). *J. Appl. Phys.* 61: 354.

41 Nakashima, S., Harima, H., Ohtani, N., and Katsuno, M. (2004). *J. Appl. Phys.* 95: 3547.
42 Matsumoto, T., Nishizawa, S., and Yamasaki, S. (2010). *Mater. Sci. Forum* 645–648: 247.
43 Sasaki, S., Suda, J., and Kimoto, T. (2012). *Mater. Sci. Forum* 717–720: 481.
44 Drowart, J., de Maria, G., and Inghram, M.G. (1958). *J. Chem. Phys.* 29: 1015.
45 Dold, P. (2015). *Advances in Photovoltaics: Part 4, Semiconductors and Semimetals*, vol. 92 (eds. G.P. Willeke and E.R. Weber), 13. Waltham, MA: Academic Press.
46 Hock, R., Konias, K., Perdicaro, L. et al. (2010). *Mater. Sci. Forum* 645–648: 29.
47 Hull, D. and Bacon, D.J. (1984). *Introduction to Dislocations*, 3e, 58. Oxford: Pergamon Press.